Progress In Electromagnetics Research, Vol. 140, 63–89, 2013

IMAGING ENHANCEMENT OF STEPPED FREQUENCY RADAR USING THE SPARSE RECONSTRUCTION TECHNIQUE

Bo Pang[1, 2, *], Da-Hai Dai[1, 2], Shi-Qi Xing[1, 2], Yong-Zhen Li[1, 2], and Xue-Song Wang[1, 2]

[1]School of Electronic Science and Engineering, National University of Defense Technology, Changsha 410073, China

[2]State Key Laboratory of Complex Electromagnetic Environment Effects on Electronics and Information System, Changsha 410073, China

Abstract—Based on the observation that sparsity assumption is well satisfied in the synthetic aperture radar (SAR) imaging applications, there is increasing interest in utilizing compressive sensing (CS) in SAR imaging. However, there are still several problems which should be concerned in CS-based imaging approaches. Firstly, inevitable noise and clutter challenge the performance of CS algorithms. Secondly, the super-resolving ability of CS algorithms is not sufficiently exploited in most cases. Thirdly, nonideal characteristics of mutual coherence affect the performance of CS algorithms in complex scenes. In this paper, a novel CS imaging framework is proposed for the purpose of improving the imaging performance of stepped frequency SAR. Meanwhile, a super-resolving imaging algorithm is proposed based on the nonquadratic optimization technique. Simulated and rail SAR measured data are applied to demonstrate the effectiveness of the novel framework with the proposed super-resolving algorithm. Experimental results validate the superiority of this method over previous approaches in terms of robustness in low SNR, better super-resolving ability and improved imaging performance in complex scenes.

Received 4 March 2013, Accepted 29 April 2013, Scheduled 22 May 2013

* Corresponding author: Bo Pang (pangbo84826@126.com).

1. INTRODUCTION

Synthetic aperture radar (SAR) is a microwave sensor which is capable of producing high-resolution images of the earth's surface [1–5]. Having the advantage of weather independence and all-day operation capability, it is widely used in many military and civilian applications [6–8].

Conventional SAR imaging schemes usually process the received signal using matched filter (MF) [9–11]. Although they are easy to implement, one common shortcoming of these MF based schemes is the resolution limitation to system bandwidth, which complicates localization of point scatterers for automated recognition tasks. In order to overcome this disadvantage, linear frequency modulation (LFM) and stepped frequency (SF) waveforms are often utilized for generating wide bandwidth. Compared to LFM waveform, the SF waveform reduces the requirement on hardware and thus has been widely employed to increase system bandwidth. Unfortunately, as there exists some tradeoff between resolution and imaging range width [12], the bandwidth of SF system can not be increased infinitely. Therefore, how to acquire super-resolution imaging ability under limited bandwidth has attracted widespread concerns in recent years.

One idea to overcome this limit is to use compressed sensing (CS) theory. As an emerging technique, CS has brought about a breakthrough to sparse signal reconstruction. According to this theory, the exact recovery of an unknown sparse signal can be achieved from limited measurements by solving a sparsity constrained optimization problem. Furthermore, this method possesses super-resolving ability, overcoming the limitation imposed by bandwidth and synthetic aperture [13]. Recent publications have shown the great potential of CS theory in various applications. In [14], it is argued that a radar system can eliminate the need for the matched filter in the radar receiver and reduce the required receiver analog-to-digital conversion bandwidth by utilizing CS theory. In [15, 16], CS theory is applied to ground penetrating radar imaging, although only a small subset of the measurements are used, the CS theory still obtains sparser and sharper target images compared to the standard back-projection method. For wide-angle imaging, where the isotropic point scattering assumption is violated, the CS is employed to improve the resolution [17, 18]. In tomographic SAR (Tomo-SAR), CS theory is exploited to overcome the poor resolution and aliasing effect brought by limited overall baseline and non-uniform inter-track distance, and better tomographic reconstruction results of man-made objects such as buildings and stadiums have been acquired [13, 19]. For SAR imaging, especially the imaging of man-made targets, the scattered signal can be deemed as a few point-like scatterers' contributions. In this sense, sparsity assumption is well satisfied for SAR imaging [20], which paves the way for utilizing CS theory in SAR imaging. However, there are still several problems that should be concerned.

Firstly, some researchers have realized the problem that the performance of CS-based imaging algorithms degrades as the SNR decreases [21, 22]. Therefore, how to obtain robust reconstruction in the presence of strong noise is challenging. Secondly, there are various methods to implement CS imaging, such as basis pursuit (BP) [23], matching pursuit (MP) [24], orthogonal matching pursuit (OMP) and so on. Among them, the OMP and its variations are most widely used for their convenience and effectiveness [1, 25–27]. Nevertheless, as special cases of greedy methods, the super-resolving abilities of OMP and its variations are poor [21, 28], i.e., the super-resolving ability of CS is not exploited sufficiently in many occasions. Thirdly, rather than realistic SAR scenes, simple and clean test scenes are usually investigated [29–31]. In these scenes, simple targets such as several isolated point scatterers take up only a small part of the scene, while the rest part of the scene is free of strong targets. In this case, only the small part of the scene including strong targets should be investigated and the influence from other parts of the scene can be negligible, which is too ideal.

Aiming at aforementioned problems, this paper focuses on the improvement of SF SAR imaging quality based on the CS theory. The contribution of this paper can be summarized as follows. Firstly, we propose a new CS imaging framework for SF SAR imaging, in which an operator is introduced to counter the influence of noise or clutter. Secondly, in order to exploit the super-resolving ability of the CS algorithms sufficiently, we provide an extension of the nonquadratic optimization technique [32] which was proposed by Cetin to the application of SAR imaging. Consequently, the super-resolving ability of the proposed algorithm is much better than that of OMP and MF based algorithms. Thirdly, in the proposed framework, the mutual coherency characteristic is more satisfactory. Therefore, even if a complex scene considered, the influence from other targets can be excluded. In this paper, a complex scene including a vehicle and some trihedral corner reflectors is investigated, and better imaging results are obtained using the proposed framework.

2. SIGNAL MODEL

In SF SAR, wide bandwidth is generated with a series of pulses with carrier frequencies increasing from pulse to pulse. Therefore, we do not require the wide instantaneous bandwidth, which will mitigate the hardware burden for the radar system. Assuming the SF signal transmitted by radar is

$$s_T(\tau) = w_r\left(\frac{\tau}{T_p}\right)\exp\left(j2\pi f_\tau(m)\,\tau\right) \tag{1}$$

where $f_\tau(m) = f_0 + m\Delta f$ denotes the carrier frequency of mth pulse; f_0 is the start carrier frequency; Δf is the frequency step; the range of m is $1 \sim B/\Delta f$ and B stands for the synthetic bandwidth; T_p is the pulse width; τ is the range time; $w_r(\tau/T_p)$ is the envelope of transmitted pulse which is usually chosen as rectangular pulse or LFM pulse signal as described in Figure 1.

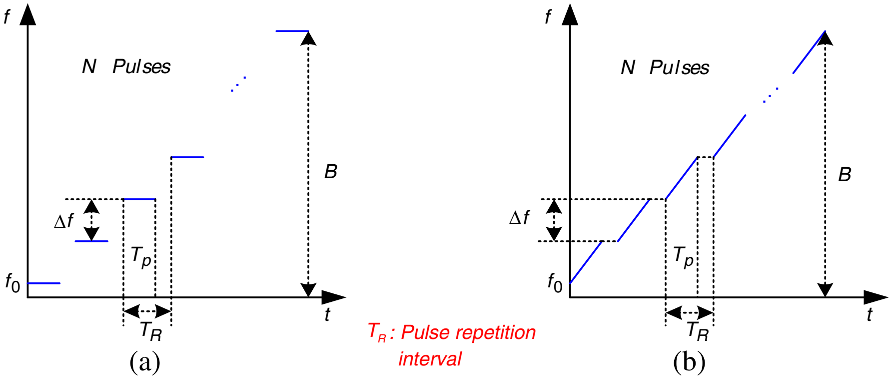

Figure 1. Two kinds of time-frequency profiles for stepped frequency radar. (a) Rectangular pulse envelope, (b) LFM pulse envelope.

For a point scatterer situated at (x, y), its echo can be expressed as

$$\begin{aligned} s_R(\tau, t) \;=\; & g(x,y)w_r\left(\frac{\tau - 2R(t;x,y)/c}{T_p}\right)w_a\left(\frac{t-y/v}{T_s}\right) \\ & \exp\left(j2\pi f_\tau(m)\left(\tau - \frac{2R(t;x,y)}{c}\right)\right) \end{aligned} \tag{2}$$

where c is the velocity of light; t is the slow time; $w_a((t - y/v)/T_s)$ is the azimuth envelope (azimuth beam pattern); T_s is synthetic aperture time; v is velocity of radar platform; $g(x, y)$ denotes the reflectivity amplitude of the target situated at (x, y) and x stands for range coordinate, y stands for azimuth coordinate; $R(t, x, y) = \sqrt{x^2 + (vt - y)^2}$ is the traveling path of electromagnetic wave from radar to target at slow time t.

Taking $s_{ref}(\tau, t) = \exp(j2\pi f_\tau(m)\tau)$ as the reference signal, the demodulated signal can be expressed as

$$\begin{aligned} s_{RD}(\tau, t) &= s_R(\tau, t) s^*_{ref}(\tau, t) \\ &= g(x,y) w_r\left(\frac{\tau - 2R(t;x,y)/c}{T_p}\right) w_a\left(\frac{t - y/v}{T_s}\right) \exp\left(-j\frac{4\pi f_\tau(m)R(t;x,y)}{c}\right) \end{aligned} \tag{3}$$

where the superscript * stands for conjugate. In order to take advantages of digital signal processing, the demodulated signal should be sampled at range time to get discrete signal. Assuming rectangular pulse envelope is used, the range time sampled signal can be expressed as

$$s_{RD}\left(f_\tau, t\right) = g\left(x, y\right) w_a\left(\frac{t - y/v}{T_s}\right) \exp\left(-j\frac{4\pi f_\tau\left(m\right) R\left(t; x, y\right)}{c}\right) \tag{4}$$

Then, we perform the Fourier transform on $s_{RD}(f_\tau,\, t)$ and get the expression of two-dimensional frequency spectrum as

$$\begin{aligned} s_{RD}\left(f_\tau, f_t\right) = g\left(x, y\right) w_a &\left(-\frac{cxf_t}{T_s\left(2v^2 f_\tau\left(m\right)\sqrt{1 - \frac{c^2 f_t^2}{4v^2 f_\tau^2(m)}}\right)}\right) \\ &\exp\left(-j\frac{4\pi x f_\tau(m)}{c}\sqrt{1 - \frac{c^2 f_t^2}{4v^2 f_\tau^2(m)}}\right) \exp\left(-j2\pi\frac{y}{v}f_t\right) \end{aligned} \tag{5}$$

Up to now, the signal model for a point target situated at (x, y) has been derived. Nevertheless, for a scene consisting of many targets, the measured signal should be represented as a superposition of the echoes reflected from all targets which are illuminated by the radar's beam. In this sense, the received signal should be written as

$$\begin{aligned} s_{RD}(f_\tau, f_t) = \iint_{\mathbf{G}} g(x, y) w_a &\left(-\frac{cxf_t}{T_s\left(2v^2 f_\tau(m)\sqrt{1 - \frac{c^2 f_t^2}{4v^2 f_\tau^2(m)}}\right)}\right) \\ &\exp\left(-j\frac{4\pi x f_\tau(m)}{c}\sqrt{1 - \frac{c^2 f_t^2}{4v^2 f_\tau^2(m)}}\right) \exp\left(-j2\pi\frac{y}{v}f_t\right) dxdy \end{aligned} \tag{6}$$

where $\mathbf{G}$ stands for the scene illuminated by the radar's beam.

In order to apply CS algorithm to two-dimensional SAR imaging, the two-dimensional distribution of targets' reflectivity should be sampled to get the discrete form as

$$\mathbf{G}=\begin{bmatrix} g\left(x_1,y_1\right) & \dots & g\left(x_1,y_Q\right)\\ \vdots & \ddots & \vdots \\ g\left(x_P,y_1\right) & \dots & g\left(x_P,y_Q\right)\end{bmatrix} \tag{7}$$

where P is the number of samples in range direction and Q the number of samples in azimuth direction. For the purpose of super-resolving, the sample interval should be smaller than the Fourier resolution cell. In the following experiments, the sample interval is chosen as one-third of the Fourier resolution cell. Therefore, P and Q are usually large numbers.

Based on (7), the received signal in (6) can be expressed as

$$s_{RD}(f_\tau(m),f_t)=\sum_{p=1}^{P}\sum_{q=1}^{Q} g(x_p,y_q)w_a\left(-\frac{cx_pf_t}{T_s\left(2v^2f_\tau(m)\sqrt{1-\frac{c^2f_t^2}{4v^2f_\tau^2(m)}}\right)}\right)$$
$$\exp\left(-j\frac{4\pi x_pf_\tau(m)}{c}\sqrt{1-\frac{c^2f_t^2}{4v^2f_\tau^2(m)}}\right)\exp\left(-j2\pi\frac{y_q}{v}f_t\right) \tag{8}$$

Following, the two-dimensional signal shown in (8) are sampled in the f_t direction (the signal is already discrete in the f_τ direction) to get

$$s_{RD}(m,n)=\sum_{p=1}^{P}\sum_{q=1}^{Q} g(x_p,y_q)w_a\left(-\frac{cx_pf_t(n)}{T_s\left(2v^2f_\tau(m)\sqrt{1-\frac{c^2f_t^2(n)}{4v^2f_\tau^2(m)}}\right)}\right)$$
$$\exp\left(-j\frac{4\pi x_pf_\tau(m)}{c}\sqrt{1-\frac{c^2f_t^2(n)}{4v^2f_\tau^2(m)}}\right)\exp\left(-j2\pi\frac{y_q}{v}f_t(n)\right) \tag{9}$$

After that, the two-dimensional signals $s_{RD}(m,\, n)$ and $g(x_p,\, y_q)$ are expressed in lexicographically ordered vector as

$$\mathbf{s}_{RD}=\begin{bmatrix} s_{RD}(1,1)\\ \vdots\\ s_{RD}(N,1)\\ \vdots\\ s_{RD}(1,M)\\ \vdots\\ s_{RD}(N,M)\end{bmatrix}\qquad \mathbf{g}=\begin{bmatrix} g(x_1,y_1)\\ \vdots\\ g(x_P,y_1)\\ \vdots\\ g(x_1,y_Q)\\ \vdots\\ g(x_P,y_Q)\end{bmatrix} \tag{10}$$

where $\mathbf{s}_{RD}$ is a $MN \times 1$ vector, $\mathbf{g}$ is a $PQ \times 1$ vector.

Then Equation (9) can be expressed as

$$\mathbf{s}_{RD} = \mathbf{A}\mathbf{g} \tag{11}$$

where $\mathbf{A}$ is a $MN \times PQ$ dictionary which can be expressed as

$$\mathbf{A} = \left[\mathbf{a}\left(1,1\right), \ldots \mathbf{a}\left(N,1\right), \ldots, \mathbf{a}\left(1,M\right), \ldots \mathbf{a}\left(N,M\right)\right]^T \tag{12}$$

where the superscript T stands for transpose.

$$\begin{aligned}\mathbf{a}\left(m,n\right) &= \left[a\left(m,n,1,1\right), \ldots, a\left(m,n,P,1\right), \ldots,\right.\\ &\qquad \left. a\left(m,n,1,Q\right), \ldots, a\left(m,n,P,Q\right)\right]^T\end{aligned} \tag{13}$$

$$\begin{aligned}a(m,n,p,q) = w_a&\left(-\frac{cx_p f_t(n)}{T_s\left(2v^2 f_\tau(m)\sqrt{1-\frac{c^2 f_t^2(n)}{4v^2 f_\tau^2(m)}}\right)}\right)\\ &\exp\left(-j\frac{4\pi x_p f_\tau(m)}{c}\sqrt{1-\frac{c^2 f_t^2(n)}{4v^2 f_\tau^2(m)}}\right)\exp\left(-j2\pi\frac{y_q}{v}f_t(n)\right)\end{aligned} \tag{14}$$

In the presence of noise, we should solve equations

$$\mathbf{s}_{RD} = \mathbf{A}\mathbf{g} + \mathbf{n} \tag{15}$$

to reconstruct the two-dimensional distribution of the targets' reflectivity $\mathbf{g}$. Since the set of equations in (15) are conventionally underdetermined, the CS theory is usually resorted to.

3. CS THEORY

According to CS theory, it is possible to recover sparse signal from a number of measurements which are much less than the number of Nyquist rate samples. Nevertheless, the key condition for CS theory to hold up lies in the sparsity or compressibility of the signal. A vector $\mathbf{x} \in \mathbf{C}^L$ is said to be K sparse when there exists a basis $\boldsymbol{\Psi}$ satisfying $\mathbf{x} = \boldsymbol{\Psi}\mathbf{s}$ while $\mathbf{s} \in \mathbf{C}^L$ has only $K \ll L$ nonzero elements. Comparing to sparsity, compressibility requires the elements of $\mathbf{s}$ follow a power decay law with K strongest coefficients [33], which is less rigorous and can be satisfied by more real-world signals.

Now, let us consider a measurement matrix (sensing matrix) $\boldsymbol{\Phi} \in \mathbf{C}^{M\times L}$ with $M \ll L$, then the measurement equations can be written as

$$\mathbf{y} = \boldsymbol{\Phi}\boldsymbol{x} = \boldsymbol{\Phi}\boldsymbol{\Psi}\mathbf{s} = \boldsymbol{\Theta}\mathbf{s} \tag{16}$$

where $\boldsymbol{\Theta} = \boldsymbol{\Phi}\boldsymbol{\Psi}$ is called dictionary. However, since this set of equations is underdetermined, exact solution of $\mathbf{s}$ from Equation (16) is challenging. In mathematical sense, underdetermined equations have infinitely many solutions. Within CS theory, the K sparse vector can be estimated from $M \geq O(K \cdot \log L)$ measurements by utilizing the sparsity of the signal, which means solving the following optimization problem:

$$(P_0) \quad \tilde{\mathbf{s}}_{CS} = \arg\min_{\mathbf{s}} \|\mathbf{s}\|_0 \quad \text{subject to} \quad \mathbf{y} = \boldsymbol{\Theta} \boldsymbol{s} \tag{17}$$

where, $\|\mathbf{s}\|_0$ returns the number of nonzero elements in the vector $\mathbf{s}$. Unfortunately, (P_0) is a N-P hard problem and is computational difficult. Instead, the problem is usually solved by a relaxed version

$$(P_1) \quad \tilde{\mathbf{s}}_{CS} = \arg\min_{\mathbf{s}} \|\mathbf{s}\|_1 \quad \text{subject to} \quad \mathbf{y} = \boldsymbol{\Theta} \mathbf{s} \tag{18}$$

where $\|\mathbf{s}\|_1$ returns the sum of the absolute values of all the elements in the vector $\mathbf{s}$.

In practice, the noise and clutter from measuring and background are inevitable, therefore the actual problem we should solve is

$$(P_1^{\varepsilon}) \quad \tilde{\mathbf{s}}_{CS} = \arg\min_{\mathbf{s}} \|\mathbf{s}\|_1 \quad \text{subject to} \quad \|\mathbf{y} - \boldsymbol{\Theta} \mathbf{s}\|_2 \leq \varepsilon \tag{19}$$

where ε stands for the noise level.

From above discussion, it is possible to note that (P_1) is the approximate solution of (P_0) and (P_1^{ε}) takes the influence of noise into account. Two natural questions are whether the approximation holds up and what is the performance of the algorithm in the presence of noise. One sufficient condition for both (P_0) and (P_1) to have the same solution and for (P_1^{ε}) to stably recover the sparse signal in the presence of noise is known as the restricted isometry property (RIP). A matrix $\boldsymbol{\Theta}$ is said to satisfy the RIP provided there exists a constant $\delta_s \in (0, 1)$ making

$$(1 - \delta_s) \|\mathbf{v}\|_2^2 \leq \|\boldsymbol{\Theta} \mathbf{v}\|_2^2 \leq (1 + \delta_s) \|\mathbf{v}\|_2^2 \tag{20}$$

holds up for any K sparse vector $\mathbf{v}$. The RIP essentially states that any subsets of K column chosen from $\boldsymbol{\Theta}$ are nearly orthogonal. Generally, the smaller δ_s, the better noise resistance performance of the algorithm.

However, in practice, there is no computational feasible way to check RIP properly, as it is combinatorial in nature [20]. Fortunately, there exist some alternatives. One of them is mutual coherence, which is defined as

$$\mu(\boldsymbol{\Theta}) = \max_{i \neq j} \frac{|\langle \boldsymbol{\rho}_i, \boldsymbol{\rho}_j \rangle|}{\|\boldsymbol{\rho}_i\|_2 \|\boldsymbol{\rho}_j\|_2} \tag{21}$$

where $\boldsymbol{\rho}_i$ stands for the ith column of matrix $\boldsymbol{\Theta}$. From another aspect, the mutual coherence can be viewed as the largest off-diagonal element of matrix $\tilde{\mathbf{\Theta}}^H\tilde{\mathbf{\Theta}}$, where $\tilde{\mathbf{\Theta}}$ is obtained by normalizing each column of $\mathbf{\Theta}$ [34]; superscript H denotes the complex conjugate.

However, the mutual coherence $\mu(\mathbf{\Theta})$ only provides the largest coherence between different columns of $\mathbf{\Theta}$, which occurs between two close columns. In other words, mutual coherence $\mu(\mathbf{\Theta})$ only describes the local characteristic of $\tilde{\mathbf{\Theta}}^H\tilde{\mathbf{\Theta}}$ but not its full characteristics. It is suitable when targets only take up a small part of the scene, while the rest part of the scene is free of strong targets. Nevertheless, when a large scene which comprises targets deployed dispersively in it is investigated, the influence of other targets (i.e., the coherence between other columns) can not be negligible. In this situation, the mutual coherence $\mu(\mathbf{\Theta})$ is not sufficient to ensure stable reconstruction.

In this paper, the full characteristics of matrix $\tilde{\mathbf{\Theta}}^H\tilde{\mathbf{\Theta}}$ are investigated but not only its largest off-diagonal element. Comparing to $\mu(\mathbf{\Theta})$, $\tilde{\mathbf{\Theta}}^H\tilde{\mathbf{\Theta}}$ is more robust in predicting the performance of the CS algorithm, especially in situation where a large scene comprises targets deployed dispersively in it. In the following sections, it can be noted that the mutual coherence characteristic is improved by the proposed algorithm.

4. NUMERICAL ITERATIVE SUPER-RESOLVING IMAGING ALGORITHM

As mentioned earlier, the MF based algorithms face the problem of Fourier resolution limited by the radar bandwidth and synthetic aperture. Nevertheless, the radar resolution is very important to the understanding of the image, especially for the application to man-made structures, which motivates the approaches for enhanced resolution.

The super-resolving ability of CS algorithm has been represented in many literatures [32, 35, 36]. However, there are various implementations for CS, and the resolving abilities of different implementations differ. For example, the OMP and its variations are widely exploited for their convenience and effectiveness. However, the super-resolving ability of these algorithms are poor [21]. In this paper, a regularization method is proposed based on nonquadartic optimization technique proposed by cetin [32]. The derivation of this algorithm can be summarized as follows.

First, we formulate the imaging problem as the following regularization problem

$$\hat{\mathbf{g}} = \arg\min_{\mathbf{g}} \left(\|\mathbf{s}_{RD} - \mathbf{A}\mathbf{g}\|_2^2 + \mu \|\mathbf{g}\|_k^k \right) \tag{22}$$

where term $\|\mathbf{s}_{RD} - \mathbf{A}\mathbf{g}\|_2^2$ is used for preserving the data fidelity of the solution; μ is the scalar parameter to balance the emphasis on data fidelity or signal energy; $\|\cdot\|_k$ denotes the l_k-norm. In this algorithm, we constraint $k \leq 1$ since the smaller value of k implies less penalty on large pixel values as compared to larger k and results in better preservation of the scatter magnitudes [32].

In a following, we denote

$$J(\mathbf{g}) = \|\mathbf{s}_{RD} - \mathbf{A}\mathbf{g}\|_2^2 + \mu \|\mathbf{g}\|_k^k \tag{23}$$

as the objective function. In order to minimize $J(\mathbf{g})$, we should first calculate the differential of $J(\mathbf{g})$ with respect to $\mathbf{g}$. However, in order to eliminate the nondifferentiablity of the l_k-norm around the origin when $k \leq 1$, $J(\mathbf{g})$ should be modified as

$$J(\mathbf{g}) = \|\mathbf{s}_{RD} - \mathbf{A}\mathbf{g}\|_2^2 + \mu \sum_{i=1}^{PQ} \left(|g_i|^2 + \xi\right)^{k/2} \tag{24}$$

where ξ is a constant small enough not to affect $\|\mathbf{g}\|_k^k$ and is chosen as $\xi = 10^{-5}$ in our experiment. Then the differential of $J(\mathbf{g})$ can be expressed as

$$\nabla J(\mathbf{g}) = \mathbf{H}(\mathbf{g})\,\mathbf{g} - 2\mathbf{A}^H \mathbf{s}_{RD} \tag{25}$$

where $\mathbf{H}(\mathbf{g}) = (2\mathbf{A}^H\mathbf{A} + \mu k \mathbf{\Lambda}(\mathbf{g}))$, superscript H denotes the complex conjugate, $\mathbf{\Lambda}(\mathbf{g}) = \operatorname{diag}\{1/(|g_i|^2 + \xi)^{1-\frac{k}{2}}\}$. The objective is to find a $\mathbf{g}$ satisfying $\nabla J(\mathbf{g}) = 0$. Noting that $\mathbf{H}(\mathbf{g})$ is the function of unknown targets' scattering reflectivity $\mathbf{g}$, we can not simply obtain the estimation of $\mathbf{g}$ by letting $\mathbf{g} = 2\mathbf{H}^{-1}(\mathbf{g})\mathbf{A}^H\mathbf{s}_{RD}$. Instead, an iterative algorithm should be utilized for solving this problem. Examining the gradient expression of (25), $\mathbf{H}(\mathbf{g})$ resembles as a "coefficient" matrix multiplying $\mathbf{g}$. Consequently, $\mathbf{H}(\mathbf{g})$ is taken as the Hessian matrix. Then the iterative algorithm can be expressed as

$$\mathbf{g}_{n+1} = \mathbf{g}_n - \mathbf{H}^{-1}(\mathbf{g}_n)\,\nabla J(\mathbf{g}_n) \tag{26}$$

We terminate iteration (26) when $\|\mathbf{g}_{n+1} - \mathbf{g}_n\|_2^2/\|\mathbf{g}_n\|_2^2 < \delta$. Where δ is a small positive termination constant and is set as $\delta = 10^{-6}$ in our experiment. The geometry demonstration of this iterative algorithm is shown in Figure 2.

Another idea to overcome the resolution limit is to use modern spectral estimation methods such as MUSIC (Multiple Emitter Location and Signal Parameter Estimation), ESPRIT (Estimation of Signal of Parameters Via Rotational Invariance Techniques) rather than MF based methods. The modern spectral estimation achieves super resolution in direction of arrival (DoA). Images generated by these approaches are inherently free of sidelobes, and the resolution

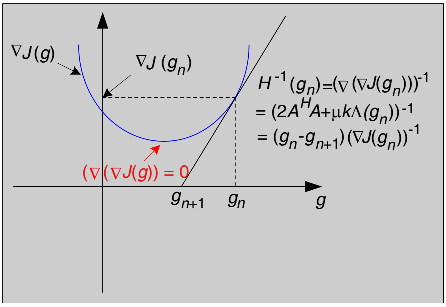

Figure 2. Geometry demonstration of the iterative algorithm.

relies on the precision of estimation. Wherein, ESPRIT [37, 38] exploits the rotational invariance of sub-array to realize the estimation of DoA. Comparing with MUSIC, ESPRIT has the advantage of computational efficiency, and eliminates the demand of spectral peak searching. Furthermore, the ESPRIT algorithm can achieve the Cramer-Rao lower bound (CRLB) on location error variance for the sum-of-reflectors model with sufficiently high signal-to-noise ratio [39, 40]. Therefore, in this paper, the super-resolving results of ESPRIT are provided to demonstrate the super-resolving ability of the proposed algorithm.

From above discussion, it can be noted that the proposed algorithm is an iterative frequency domain CS algorithm. Therefore, for simplicity, it is acronymized as IFCS in the following discussion.

5. EXPERIMENT RESULTS

In this section, the superiority of IFCS is demonstrated using simulated and real data. The imaging results of Omega-K algorithm and time domain CS (i.e., the CS theory is applied directly to the time domain echo) imaging algorithm proposed in [12] are also represented for comparison. Among them, Omega-K [41–43] algorithm is a representative MF based imaging algorithm. Since the data are processed in the 2D frequency domain with little approximations in Omega-K algorithm, it is often deemed as an accurate algorithm and used as a reference to evaluate other imaging algorithms.

5.1. Noise Resistant Capability

Firstly, we demonstrate the noise resistant capability of IFCS on a simple simulated scene which consists of four point scatterers

Table 1. Scatterer properties.

	Range	Azimuth	Amplitude
Scatter 1	54.5	0	0.5
Scatter 2	52.4	0	1
Scatter 3	56	1.5	0.3
Scatter 4	55.4	−1.5	1

Table 2. Simulation parameters.

Parameter	Value
Carrier Frequency	10 GHz
Bandwidth	500 MHz
Radar Velocity	0.1 m/s
Frequency Step	1 MHz
Sweep Period	120 ms
Radar Height	2.5 m
Azimuth Beam Width	2.5°

with different reflectivity amplitude. The coordinate and reflectivity amplitude of these scatterers are listed in Table 1. The simulation parameters are listed in Table 2.

Figure 3 shows the color-coded (color are coded by the reflectivity amplitude of the scatterers) imaging results of the simulated scene with different imaging algorithms. For IFCS, the parameters are chosen as $k = 0.1$ and $\mu = 1000$ empirically. Considering the inevitable noise from measuring and background, the simulated data are added with white Gaussian noise, which is commonly used for radar measurement noise. From up to down, the SNR levels are 0 dB, 10 dB and −10 dB respectively.

From the color-coded images shown in Figure 3(a) to Figure 3(c), it can be noted that when SNR is high, both the time domain CS algorithm and IFCS can reconstruct the scatterers well. Namely not only the positions of scatterers are correctly reconstructed but also their reflectivity amplitude information is well preserved. Furthermore, comparing to the imaging result of the Omega-K algorithm, the absence of sidelobes makes the images generated by the time domain CS and IFCS much preferable, considering that the sidelobes will prevent a better discrimination of closely located targets. However, when SNR degrades to 0 dB, artifacts will appear in image provided

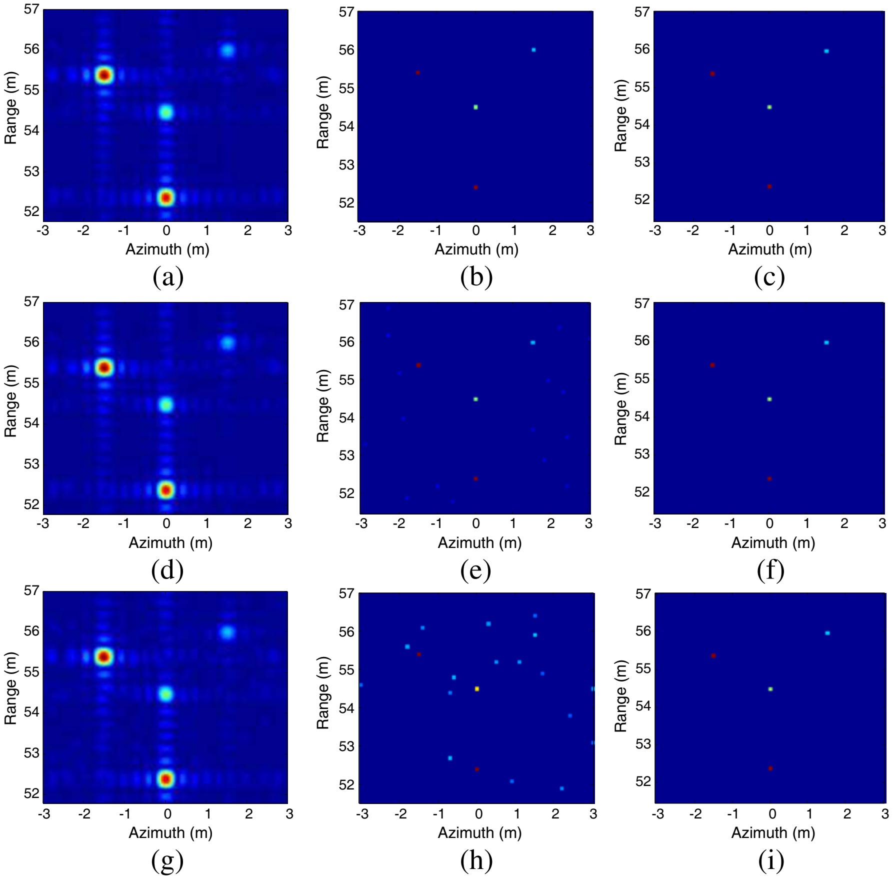

Figure 3. Color-coded imaging results of a simulated scene with 4 scatterers having different reflectivity amplitudes under different SNR levels, color is coded by the reflectivity amplitude of the scatterers. (Upper plots) SNR = 10 dB. (Middle plots) SNR = 0 dB. (Lower plots) SNR = −10 dB. (a) Omega-K, (b) time domain CS, (c) IFCS, (d) Omega-K, (e) time domain CS, (f) IFCS (g) Omega-K, (h) time domain CS, (i) IFCS.

by the time domain CS algorithm (shown in Figure 3(e)) while the image provided by IFCS is still free of artifacts (shown in Figure 3(f)). When SNR further degrades to −10 dB, the amplitude of artifacts will rise, making the weak scatterer (i.e., scatterer 3 situated at the top right part of the scene) submerged in artifacts. Nevertheless, IFCS exhibits its robustness and stability in strong noise cases (shown in

Figure 3(i)), in which targets are detected with accurate amplitudes at the right positions, and no artifacts appear.

The better noise resistant capability of IFCS can be owed to the azimuth Fourier transform included in it. After Fourier transforming, the signal energy will concentrate to several Doppler bins, while the noise energy is still spreading over the whole frequency domain, leading to the improvement of SNR. However, for the time domain CS imaging algorithm, it has been proven that the estimation error of the unknown signal is approximately proportional to the noise level [44]. Therefore, it is not difficult to understand that the performance of the time domain CS imaging algorithm degrades and artifacts increases as SNR decreases.

5.2. Super-resolving Performance

In order to evaluate the super-resolving performance of IFCS, scenes which comprises two closely separated scatterers in range/azimuth direction are simulated with the parameters listed in Table 2. Afterwards, different algorithms are applied and the imaging results are presented in Figure 4 to Figure 11. The SNR is set to 10 dB. The Fourier resolutions for range and azimuth direction are 0.3 m and 0.35 m respectively. For IFCS, the parameters are still chosen as $k = 0.1$ and $\mu = 1000$ empirically.

Firstly, the situation of two closely separated scatterers in range direction is investigated, and the results are presented in Figure 4 to Figure 7. From Figure 4 it can be noted that the Omega-K imaging

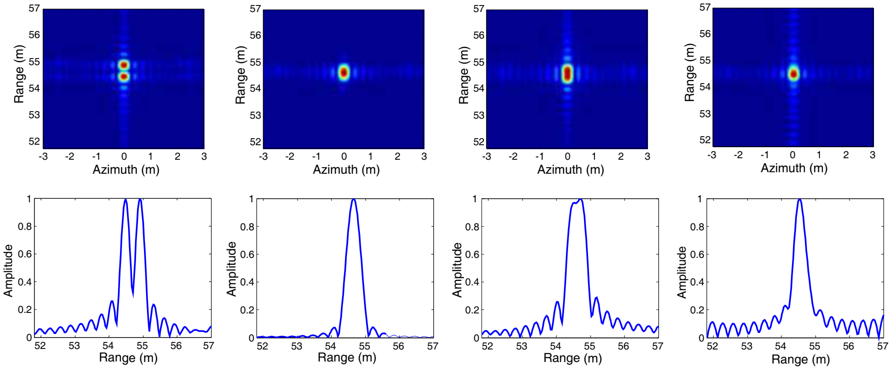

Figure 4. Imaging results of two closely separated scatterers in range direction using the Omega-K algorithm. One scatterer situated at (54.5, 0), the other one situated at (54.9, 0), (54.8, 0), (54.7, 0) or (54.6, 0) from left to right. (Upper plots) Two-dimensional imaging results. (Lower plots) Range profiles corresponding to Upper plots.

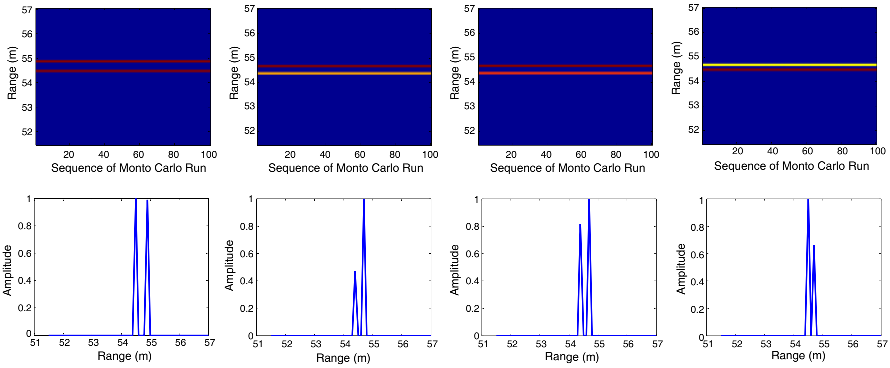

Figure 5. Imaging results of two closely separated scatterers in range direction using the OMP algorithm. One scatterer situated at (54.5, 0), the other one situated at (54.9, 0), (54.8, 0), (54.7, 0) or (54.6, 0) from left to right. (Upper plots) Range profiles of 100 Monte Carlo runs. (Lower plots) Range profile corresponding to 100th Monte Carlo Run.

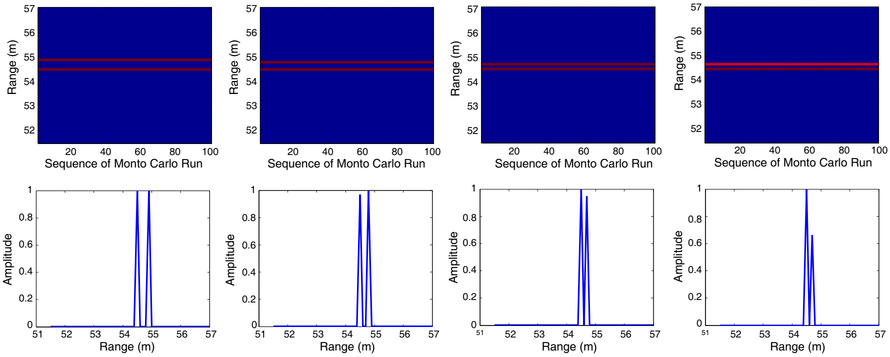

Figure 6. The imaging results of two closely separated scatterers in range direction using the IFCS algorithm. One scatterer situated at (54.5, 0), the other one situated at (54.9, 0), (54.8, 0), (54.7, 0) or (54.6, 0) from left to right. (Upper plots) Range profiles of 100 Monte Carlo runs. (Lower plots) Range profile corresponding to 100th Monte Carlo Run.

algorithm cannot resolve the scatterers falling into one resolution cell and suffers from sidelobes. Comparing to Omega-K imaging algorithm, the images obtained by the OMP algorithm is free of sidelobes. However, the super-resolving ability of the OMP algorithm is still

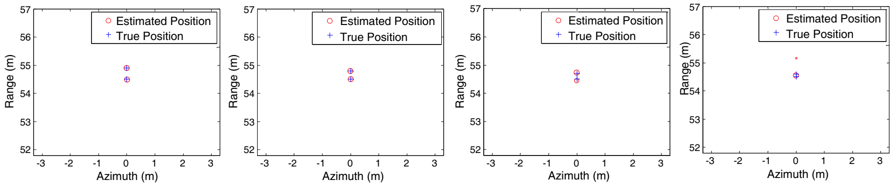

Figure 7. Imaging results of two closely separated scatterers in range direction using ESPRIT algorithm. One scatterer situated at (54.5, 0), the other one situated at (54.9, 0), (54.8, 0), (54.7, 0) or (54.6, 0) from left to right.

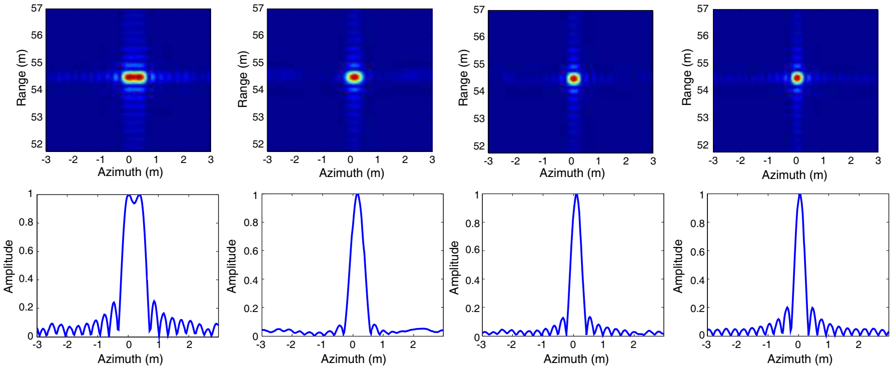

Figure 8. Imaging results of two closely separated scatterers in azimuth direction using the Omega-K algorithm. One scatterer situated at (54.5, 0), the other one situated at (54.5, 0.4), (54.5, 0.3), (54.5, 0.2) or (54.5, 0.1) from left to right. (Upper plots) Two-dimensional imaging results. (Lower plots) Range profiles corresponding to upper plots.

limited. When two scatterers move into one resolution cell, the results become unsatisfactory. Firstly, the scatterers are not right located in reconstructed images. For example, the scatterers situated at (54.5, 0) and (54.7, 0) are located at (54.4, 0) and (54.6, 0) instead. Secondly, the amplitude information of the scatterers is not well preserved by the OMP algorithm. As a result, the reconstructed amplitude of two scatterers with equal amplitude appears to have considerable discrepancy. Figure 6 shows the imaging results of IFCS. It is pleased to see that the super-resolving performance is much improved by using IFCS. Two scatterers are stably reconstructed with accurate position and amplitude until the range direction distance between them is closer than one-third Fourier resolution cell. Figure 7 shows the imaging result using the ESPRIT algorithm with *a priori* information

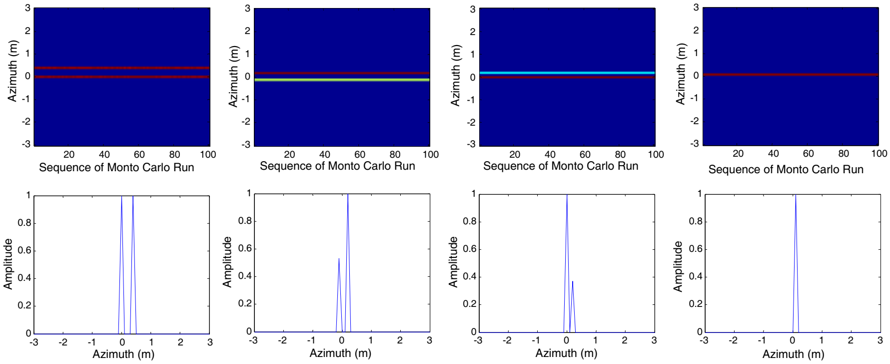

Figure 9. Imaging results of two closely separated scatterers in azimuth direction using the OMP algorithm. One scatterer situated at (54.5, 0), the other one situated at (54.5, 0.4), (54.5, 0.3), (54.5, 0.2) or (54.5, 0.1) from left to right. (Upper plots) Azimuth profiles of 100 Monte Carlo runs. (Lower plots) Azimuth profile corresponding to 100th Monte Carlo run.

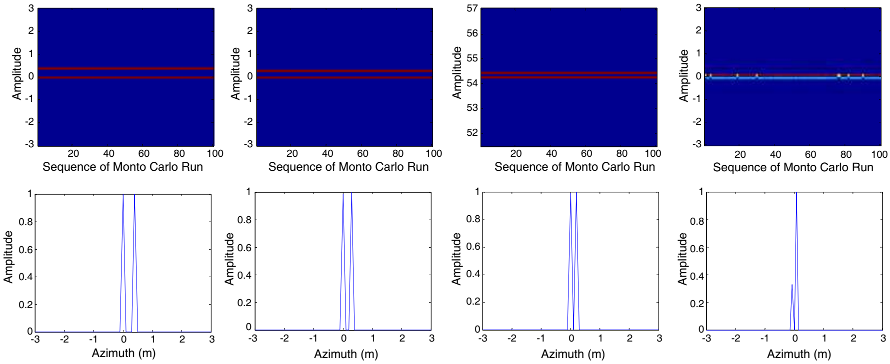

Figure 10. Imaging results of two closely separated scatterers in azimuth direction using the IFCS algorithm. One scatterer situated at (54.5, 0), the other one situated at (54.5, 0.4), (54.5, 0.3), (54.5, 0.2) or (54.5, 0.1) from left to right. (Upper plots) Azimuth profiles of 100 Monte Carlo runs. (Lower plots) Azimuth profile corresponding to 100th Monte Carlo Run.

about the number of scatterers. Blue cross and red circle stand for the true and estimated positions of the scatterers respectively while their size is directly proportional to the amplitude of the scatterers. Similarly to the results obtained using IFCS, two scatterers are well reconstructed until they are closer than one-third Fourier resolution

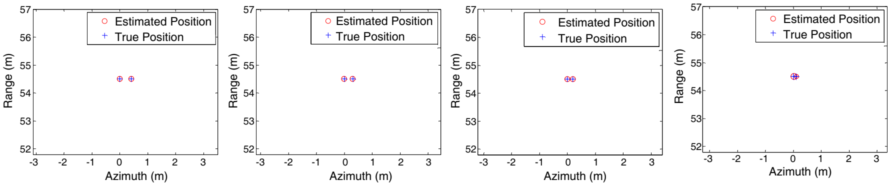

Figure 11. Imaging results of two closely separated scatterers in azimuth direction using ESPRIT algorithm. One scatterer situated at (54.5, 0), the other one situated at (54.5, 0.4), (54.5, 0.3), (54.5, 0.2) or (54.5, 0.1) from left to right.

cell, which demonstrates the super-resolving capability of IFCS from another aspect. However, comparing to the ESPRIT algorithm, IFCS eliminates the step of model order selection, i.e., IFCS "adaptively" chooses the number of scatterers.

Afterwards, the situation of two closely separated scatterers in azimuth direction is investigated. Since similar conclusion can be established, the results shown in Figure 8 to Figure 11 are not analyzed in detail here.

5.3. Improvement of Mutual Coherence Characteristics

In this section, not only the largest off-diagonal element of matrix $\tilde{\boldsymbol{\Theta}}^H\tilde{\boldsymbol{\Theta}}$, i.e., $\mu(\boldsymbol{\Theta})$, but also its full characteristics corresponding to the $5.5\,\mathrm{m} \times 6\,\mathrm{m}$ scene in Section 5.1 are investigated. Table 3 shows the parameter $\mu(\boldsymbol{\Theta})$ for the time domain CS algorithm and IFCS. It seems that if only $\mu(\boldsymbol{\Theta})$ is used for evaluation, the performance of the time domain CS algorithm and the IFCS algorithm is comparable.

Table 3. The $\mu(\boldsymbol{\Theta})$ parameter of different CS framework.

	Time domain CS	IFCS
$\mu(\boldsymbol{\Theta})$	0.31	0.34

Figure 12 shows the representation of $\tilde{\boldsymbol{\Theta}}^H\tilde{\boldsymbol{\Theta}}$. It can be noted that the elements of $\tilde{\boldsymbol{\Theta}}^H\tilde{\boldsymbol{\Theta}}$ distribute following a band crossing the matrix from the upper left corner to the bottom right corner. Theoretically, the mutual coherence decreases as the distance between the columns augments. Nevertheless, the elements of $\tilde{\boldsymbol{\Theta}}^H\tilde{\boldsymbol{\Theta}}$ exhibit some fluctuations in time domain CS framework when distance between the columns augments (shown in Figure 12(a)). On the contrary, the mutual coherence characteristic of IFCS is preferable. On one

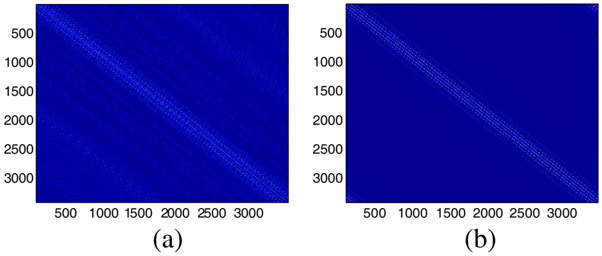

(a) (b)

Figure 12. Representation of matrix $\tilde{\boldsymbol{\Theta}}^H\tilde{\boldsymbol{\Theta}}$. (a) Time domain CS, (b) IFCS

hand, the large mutual coherence concentrate around the principal diagonal of matrix $\tilde{\boldsymbol{\Theta}}^H\tilde{\boldsymbol{\Theta}}$. On the other hand, when distance between the columns augments, the mutual coherence decreases dramatically, indicating the negligible influence from further targets. The advantage of the mutual coherence characteristic in IFCS is demonstrated in next section using measured data.

5.4. Real Data Imaging Results

In this section, the measured X-band stepped frequency SAR data are used to demonstrate the effectiveness of IFCS. The test scene located at the suburb of Changsha, China, is a slightly undulated field covered by weeds and a few bushes. In this test site, a rail SAR experiment system is established with a vector network analyzer (VNA) mounted on the platform which is moving along the rail with preset velocity. While the platform is moving, the VNA transmits SF signal and collects echoes under the control of a computer. The experiment parameters are shown in Table 4. Figure 13 presents the photograph of the rail SAR experiment system and its components.

Figure 14 shows photographs of the targets deployed in the test scene. As having the ideal point-like scattering properties and exactly scattering mechanism, the trihedral corner reflectors are widely utilized to demonstrate the performance of imaging algorithm. In our experiment, four trihedral corner reflectors are deployed in the test scene, as shown in Figure 14(c) to Figure 14(e). Trihedral corner reflector A is deployed on a metal stair with some corner structures. It is expected to be stronger in SAR image as the contribution of the metal stair included. Trihedral corner reflectors B1 and B2 are two targets which almost locate at the same azimuth. However, since B2 is deployed above ground with a height of about 1 m, these two targets separate in range direction with about 0.7 m. Trihedral corner reflector C deployed on the ground is the target closest to radar. In

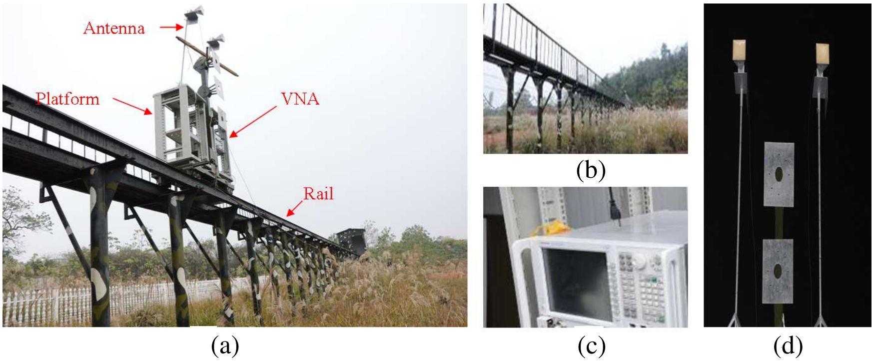

(a) (b) (c) (d)

Figure 13. The photograph of rail SAR experiment system. (a) Overview of the experiment system. (b) Rail. (c) Agilent VNA (PNX-5242A). (d) Transmitting and receiving antennas.

Table 4. Experiment parameters.

Parameter	values	Parameter	values
Carrier Frequency	10 GHz	Depression Angle	3.8°
Radar Bandwidth	500 MHz	Reference Antenna Height	4.34 m
Frequency Step	1 MHz	Intermediate Frequency Bandwidth	1 MHz
Sweep period	120 ms	Source Port Power	15 dBmw
Platform Velocity	0.1 m/s	Sweep Type	Step Frequency
Azimuth Beam Width	18°		

addition to simple corner reflectors, a more complicated target, i.e., a vehicle, is deployed in the test site to validate the performance of IFCS in reconstructing complex targets. The photograph of the vehicle is shown in Figure 14(b).

Figure 15 shows a 2D image of the test site obtained by the

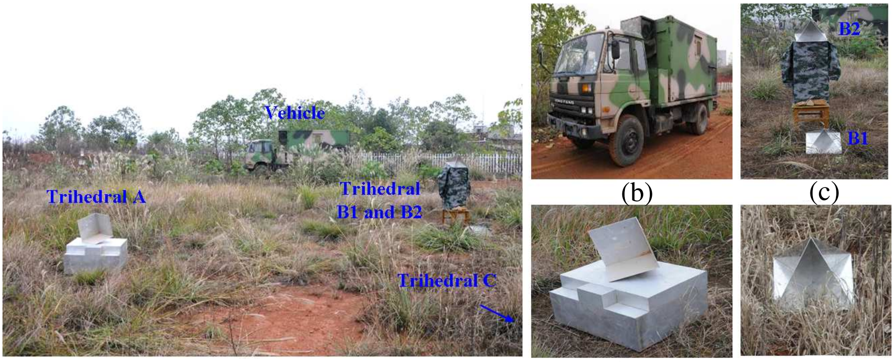

(a) (b) (c) (d) (e)

Figure 14. The photograph of targets deployed in test scene. (a) The overview of the targets. (b) The vehicle. (c) Trihedral corner reflector A. (d) Trihedral corner reflectors B1 and B2. (e) Trihedral corner reflector C.

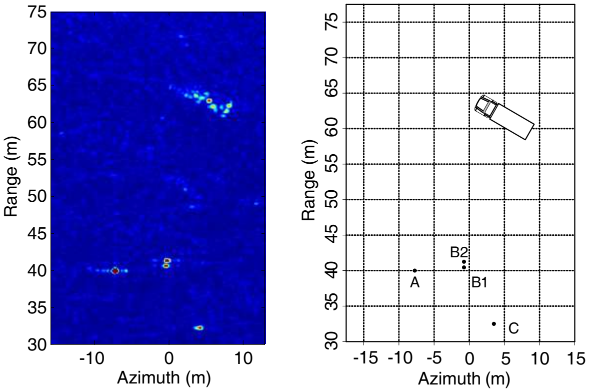

(a) (b)

Figure 15. (a) Imaging result of the test site obtained by Omega-K algorithm. (b) Ground truth.

Omega-K algorithm and the ground truth. A remarkable consistency can be found between them. Therefore, in the following discussion, the image shown in Figure 15(a) is taken as a reference to evaluate the performance of other algorithms. However, one aspect worth to describe in Figure 15(a) is the "noisy" look, especially in areas without strong point scatterers. The source of noise can be summarized as three folds. Firstly, in order to accelerate frequency scan, the intermediate

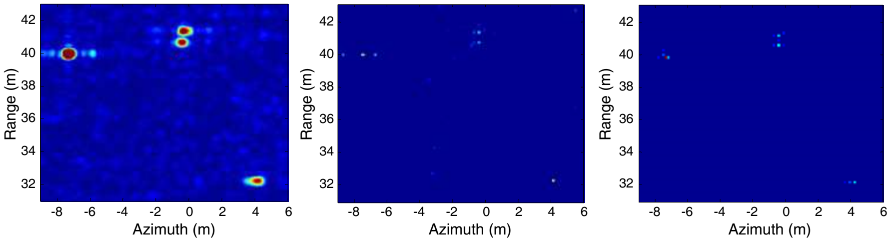

(a) (b) (c)

Figure 16. Color-coded imaging results of four corner reflectors. Color is coded by the reflectivity amplitude of the scatterers. (a) Omega-K, (b) time domain CS, (c) IFCS.

frequency bandwidth of VNA is set as 1 MHz in our experiment, which will shorten the frequency scanning period. However, the SNR is sacrificed instead. Secondly, the returns are inevitably interfered by clutter. Thirdly, as the coherent nature of SAR system, the returns are contaminated by the speckle noise.

Figure 16 shows the imaging results of four trihedral corner reflectors (A, B1, B2, C) using different algorithms. From imaging result of the Omega-K algorithm (shown in Figure 16(a)), it can be noted that trihedral corner reflector A appears to be stronger than the others, as the contribution of the metal stair included. For the time domain CS algorithm, although four trihedral corner reflectors are right reconstructed, the blurring of the image caused by some artifacts is also obvious. On the contrary, IFCS generates image with much less artifacts. Moreover, trihedral A appears to be stronger than the others, i.e., the reflectivity amplitude information is preserved by IFCS.

Figure 17 shows the imaging results of a complicated target, i.e., a

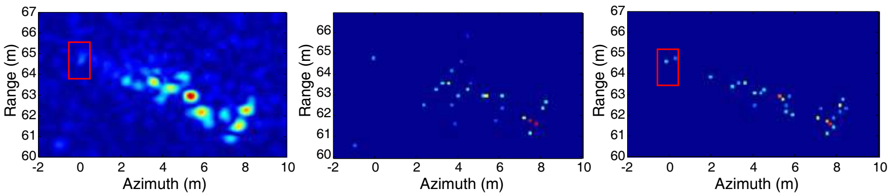

(a) (b) (c)

Figure 17. Color-coded imaging results of a vehicle. Color is coded by the reflectivity amplitude of the scatterers. (a) Omega-K, (b) time domain CS, (c) IFCS.

vehicle, using different algorithms. For the time domain CS algorithm, it can be seen that the outline and detail of the vehicle are not well preserved and the image is contaminated by some artifacts. However, the image obtained by using IFCS is much preferable. Firstly, the shape and geometry features of the vehicle are well preserved, which permits the effective use of region-based target recognition algorithm. Second, the vehicle is represented as a set of scatterers in image generated by using IFCS. Although precise super-resolving arguments are not as easy for this complicated target, IFCS seems to capture more details about the vehicle. Even some weak scattering centers such as the one corresponding to the head of the vehicle (marked as red rectangular in Figure 17(a)) which is weak in image obtained by the Omega-K algorithm is enhanced in image obtained by using IFCS. Thirdly, the sparse reconstruction obtained by CS-based algorithm has been proven to be more effective than the images obtained by the Omega-K algorithm when the automatic system is used for detection and recognition [45]. Fourth, IFCS shows its robustness in the presence of noise and clutter, as the image obtained by IFCS is dense and clean.

6. CONCLUSION

In this paper, a novel CS framework for stepped frequency SAR imaging is proposed. Meanwhile, a super-resolving algorithm (i.e., IFCS) is proposed based on the nonquadratic optimization technique in order to enhance super-resolving ability. The preferable characteristics of the proposed framework with super-resolving algorithm are firstly verified using a scene consists of four point scatterers with different reflectivity amplitudes. In addition to the absence of sidelobes, IFCS exhibits better performance than time domain CS under low SNR. Afterwards, we simulate the scenes which comprise two closely separated scatterers in range/azimuth direction to validate the super-resolving ability of IFCS. The imaging results of OMP and ESPRIT are also represented for comparison purpose. The results indicate that the super-resolving ability of IFCS outperforms OMP and is comparable to that of ESPRIT. Apart from simulated data, an X-band stepped frequency rail SAR experiment system is established to demonstrate the effectiveness of IFCS with real data. Another aspect worth to mention is that not only simple corner reflectors but also a vehicle is deployed in the test site, which is more persuadable. Consequently, in images obtained by IFCS, the corner reflectors and the vehicle are right located with accurate reflectivity and reduced artifacts. Furthermore, more details about the vehicle are captured by IFCS.

REFERENCES

1. Chan, Y. K. and V. C. Koo, "An introduction to synthetic aperture radar (SAR)," *Progress In Electromagnetics Research B*, Vol. 2, 27–60, 2008.
2. Zhang, M., Y. W. Zhao, H. Chen, and W.-Q. Jiang, "SAR imaging simulation for composite model of ship on dynamic ocean scene," *Progress In Electromagnetics Research*, Vol. 113, 395–412, 2011.
3. Sun, J., S. Mao, G. Wang, and W. Hong, "Polar format algorithm for spotlight bistatic SAR with arbitrary geometry configuration," *Progress In Electromagnetics Research*, Vol. 103, 323–338, 2010.
4. Mohammadpoor, M., et al., "A circular synthetic aperture eadar for on-the-ground object detection," *Progress In Electromagnetics Research*, Vol. 122, 269–292, 2012.
5. Koo, V. C., et al., "A new unmanned aerial vehicle synthetic aperture radar for environmental monitoring," *Progress In Electromagnetics Research*, Vol. 122, 245–268, 2012.
6. Lim, T. S., C.-S. Lim, and V. C. Koo, "Autofocus algorithm performance evaluations using an integrated SAR product simulator and processor," *Progress In Electromagnetics Research B*, Vol. 3, 315–329, 2008.
7. Storvold, R., E. Malnes, Y. Larsen, K. A. Hogda, and S. E. Hamran, "SAR remote sensing of snow parameters in Norwegian areas-current status and future perspective," *Journal of Electromagnetic Waves and Applications*, Vol. 20, No. 13, 1751–1759, 2006.
8. Li, Y., G. H. Lv, and X. Z. Liu, "Moving-target velocity estimation in a complex-valued SAR imagery," *Progress In Electromagnetics Research*, Vol. 136, 301–325, 2013.
9. Park, S.-H., J.-I. Park, and K.-T. Kim, "Motion compensation for squint mode spotlight SAR imaging using effcient 2D interpolation," *Progress In Electromagnetics Research*, Vol. 128, 503–518, 2012.
10. Liu, Y., Y. K. Deng, and R. Wang, "An extended inverse chirp-z transform algorithm to process high squint SAR data," *Progress In Electromagnetics Research*, Vol. 138, 555–569, 2013.
11. Wu, J., Z. Li, Y. Huang, Q. Liu, and J. Yang, "Processing one-stationary bistatic SAR data using inverse scaled fourier transform," *Progress In Electromagnetics Research*, Vol. 129, 143–159, 2012.
12. Yang, J. G., J. Thompson, X. T. Huang, T. Jin, and Z. M. Zhou, "Random-frequency SAR imaging based on compressed sensing,"

IEEE Trans. on Geoscience and Remote Sensing, Vol. 51, No. 2, 983–994, Feb. 2013.

13. Budillon, A., A. Evangelista, and G. Schirinzi, "Three-dimensional SAR focusing from multipass signals using compressive sampling," *IEEE Trans. on Geoscience and Remote Sensing*, Vol. 49, No. 1, 488–499, Jan. 2011.
14. Baraniuk, R. and P. Steeghs, "Compressive radar imaging," *Proc. IEEE 2007 Radar Conference*, 128–133, Waltham, MA, Apr. 2007.
15. Gurbuz, A. C., J. H. McClellan, and W. R. Scott, "Compressive sensing for GPR imaging," *Proc. 41st Asilomar Conference on Signals, Systems Computers (ACSSC)*, 2223–2227, Nov. 2007.
16. Gurbuz, A. C., J. H. McClellan, and W. R. Scott, "Compressive sensing for subsurface imaging using ground penetrating radar," *Signal Processing*, Vol. 89, No. 10, 1959–1972, 2009.
17. Austin, C. D., E. Ertin, and R. L. Moses, "Sparse signal methods for 3-D radar imaging," *IEEE Journal of Selected Topics in Signal Processing*, Vol. 5, No. 3, 408–423, Jun. 2011.
18. Varshney, K. R., M. Cetin, J. W. Fisher, and A. S. Willsky, "Sparse signal representation in structured dictionaries with application to synthetic aperture radar," *IEEE Trans. on Signal Processing*, Vol. 56, No. 8, 3548–3561, Aug. 2008.
19. Zhu, X. X. and R. Bamler, "Tomographic SAR inversion by l1-norm regularization — The compressive sensing approach," *IEEE Trans. on Geoscience and Remote Sensing*, Vol. 48, No. 10, 3839–3846, Oct. 2010.
20. Patel, V. M., G. R. Easley, D. M. Healy, and R. Chellappa, "Compressed synthetic aperture radar," *IEEE Journal of Selected Topics in Signal Processing*, Vol. 4, No. 2, 244–254, Apr. 2010.
21. Xing, S. Q., Q. F. Liu, D. H. Dai, Y. Z. Li, and X. S. Wang, "Polarimetric SAR tomography using l21 mixed norm sparse reconstruction method," *Progress In Electromagnetics Research*, Vol. 130, 105–130, 2012.
22. Zhang, L., M. D. Xing, C. W. Qiu, J. Li, J. L. Sheng, Y. C. Li, and Z. Bao, "Resolution enhancement for inversed synthetic aperture radar imaging under low SNR via improved compressive sensing," *IEEE Trans. on Geoscience and Remote Sensing*, Vol. 48, No. 10, 3824–3838, Oct. 2010.
23. Chen, S., D. Donoho, and M. A. Saunders, "Atomic decomposition by basis pursuit," *SIAM Journal on Scientific Computing*, Vol. 20, No. 1, 33–61, 1999.
24. Tropp, J. and A. Gilbert, "Signal recovery from random

measurements via orthogonal matching pursuit," *IEEE Trans. on Information Theory*, Vol. 53, No. 12, 4655–4666, Dec. 2007.

25. Needell, D. and R. Vershynin, "Greedy signal recovery and uncertainty principles," *Proc. SPIE*, Vol. 6814, J-1–J-12, Bellingham, WA, 2008.
26. Alonso, M. T., P. L. Dekker, and J. J. Mallorqui, "A novel strategy for radar imaging based on compressive sensing," *IEEE Trans. on Geoscience and Remote Sensing*, Vol. 48, No. 12, 3824–3838, Dec. 2010.
27. Needell, D. and J. A. Tropp, "CoSaMP: Iterative signal recovery from incomplete and inaccurate samples," *Appl. Comp. Harmonic Anal.*, Vol. 26, 301–321, 2008.
28. Xing, S. Q., Y. Z. Li, D. H. Dai, and X. S. Wang, "3D reconstruction of manmade objects using polarimetric tomographic SAR," *IEEE Trans. on Geoscience and Remote Sensing*, 455–458, 2012.
29. Jouny, I., "Compressed sensing for UWB radar target signature reconstruction," *IEEE 13th Digital Signal Processing Workshop and 5th IEEE Signal Processing Education (DSP/SPE) Workshop*, 714–719, 2009.
30. Herman, M. and T. Strohmer, "Compressed sensing radar," *Proc. IEEE International Conference on Acoustics, Speech and Signal Processing (ICASSP)*, 1509–1512, 2008.
31. Herman, M. and T. Strohmer, "High-resolution radar via compressed sensing," *IEEE Trans. on Signal Processing*, Vol. 57, No. 6, 2275–2284, Jun. 2009.
32. Cetin, M. and W. C. Karl, "Feature-enhanced synthetic aperture radar image formation based on nonquadratic regularization," *IEEE Trans. on Image Processing*, Vol. 10, No. 4, 623–631, Apr. 2001.
33. Candes, E., J. Romberg, and T. Tao, "Robust uncertainty principles: Exact signal reconstruction from highly incomplete frequency information," *IEEE Trans.on Information Theory*, Vol. 52, No. 2, 489–509, Feb. 2006.
34. Donoho, D., M. Elad, and V. N. Temlyakov, "Stable recovery of sparse overcomplete representations in the presence of noise," *IEEE Trans. on Information Theory*, Vol. 52, No. 1, 6–18, Jan. 2006
35. Potter, L. C., E. Ertin, J. T. Parker, and M. Cetin, "Sparsity and compressed sensing in radar imaging," *Proceedings of the IEEE*, Vol. 98, No. 6, 1006–1020, Jun. 2010.

36. Samadi, S., M. Cetin, and M. A. Masnadi-Shirazi, "Sparse representation-based synthetic aperture radar imaging," *IET Radar Sonar & Navigation*, Vol. 5, No. 2, 182–193, 2011.
37. Roy, R., A. Paulraj, and T. Kailath, "ESPRIT — A subspace rotation approach to estimation of parameters of cisoids in noise," *IEEE Trans. on Acoustics, Speech and Signal Processing*, Vol. 34, 1340–1342, Oct. 1986.
38. Roy, R. and T. Kailath, "ESPRIT — Estimation of signal parameters via rotational invariance techniques," *IEEE Trans. on Acoustics, Speech and Signal Processing*, Vol. 37, 984–995, Jul. 1989.
39. Blu, T., P.-L. Dragotti, M. Vetterli, P. Marziliano, and L. Coulot, "Sparse sampling of signal innovations," *IEEE Signal Processing Magazine*, 31–40, Mar. 2008.
40. Xing, S. Q., D. H. Dai, X. S. Wang, and T. Wang, "Two-dimensional ESPRIT super-resolution feature extraction using fully polarized measurements and its performance analysis," *Acta Electronica Sinica*, Vo1. 37, No. 12, 2681–2687, 2009.
41. Guo, D., H. Xu, and J. Li, "Extended wavenumber domain algorithm for highly squinted sliding spotlight SAR data processing," *Progress In Electromagnetics Research*, Vol. 114, 17–32, 2011.
42. Cafforio, C., C. Prati, and F. Rocca, "Full resolution focusing of SEASAT SAR images in the frequency-wave number domain," *Proc. 8th EARSel Workshop*, 336–355, May 1988.
43. Bamler, R., "A comparison of range-doppler and wavenumber domain SAR focusing algorithms," *IEEE Trans. on Geoscience and Remote Sensing*, Vol. 30, No. 4, 706–713, Jul. 1992.
44. Jafarpour, S., W. Xu, B. Hassibi, and R. Calderbank, "Efficient and robust compressed sensing using optimized expander graphs," *IEEE Trans. on Information Theory*, Vol. 55, No. 9, 4299–4308, Sep. 2009.
45. Cetin, M., W. C. Karl, and D. A. Castanon, "Feature enhancement and ATR performance using nonquadratic optimization-based SAR imaging," *IEEE Trans. on Aerospace and Electronic Systems*, Vol. 39, No. 4, 1375–1395, Oct. 2003.